View metadata, citation and similar papers at core.ac.uk

brought to you by CORE

provided by UNL | Libraries

University of Nebraska - Lincoln
DigitalCommons@University of Nebraska - Lincoln

U.S. Air Force Research | U.S. Department of Defense

2013

Optimal thickness distributions of aeroelastic flapping shells

Bret Stanford
Wright–Patterson AFB, bret.stanford@wpafb.af.mil

Philip Beran
Wright–Patterson AFB

Follow this and additional works at: http://digitalcommons.unl.edu/usafresearch


Part of the Aerospace Engineering Commons

Stanford, Bret and Beran, Philip, "Optimal thickness distributions of aeroelastic flapping shells" (2013). *U.S. Air Force Research*. 76.
http://digitalcommons.unl.edu/usafresearch/76

This Article is brought to you for free and open access by the U.S. Department of Defense at DigitalCommons@University of Nebraska - Lincoln. It has been accepted for inclusion in U.S. Air Force Research by an authorized administrator of DigitalCommons@University of Nebraska - Lincoln.

Aerospace Science and Technology 24 (2013) 116–127

Contents lists available at SciVerse ScienceDirect

Aerospace Science and Technology

www.elsevier.com/locate/aescte

Optimal thickness distributions of aeroelastic flapping shells

Bret Stanford *, Philip Beran

U.S. Air Force Research Laboratory, Wright–Patterson AFB, OH 45433, United States

ARTICLE INFO

Article history:
Received 17 September 2010
Received in revised form 24 January 2011
Accepted 25 October 2011
Available online 29 October 2011

Keywords:
Flapping wing
Aeroelasticity
Tailoring
Sensitivity analysis

ABSTRACT

The severe weight limitations of flapping wing micro air vehicles necessitates the use of thin flexible wings, which in turn requires an aeroelastic modeling tool for proper numerical characterization. Furthermore, due to the unconventional nature of these vehicles, wing design guidelines for thrust and/or power considerations are not generally available; numerical design optimization then becomes a valuable tool. This work couples a nonlinear shell model to an unsteady vortex lattice solver, and then computes analytical design gradients: the derivative of aerodynamic force/power quantities with respect to a large vector of thickness variables. Gradient-based optimization is then used to locate the wing structure that maximizes the thrust, or minimizes the power under a thrust constraint, for a variety of shell boundary conditions. Changes in the topological features of the optimal wing thicknesses highlight important aeroelastic interactions that can be exploited for efficient flapping wings.

Published by Elsevier Masson SAS.

1. Introduction

Nonlinear shell finite element modeling has attracted considerable interest within the micro air vehicle community in recent years, providing a level of fidelity very suitable for flapping wing analysis and design. Beam models have been utilized for some three-dimensional flapping studies (see Isogai and Harino [12], Beran et al. [1], Stanford et al. [24], among others), but an inability to handle chordwise deformations and pressure gradients (an important source of thrust generation via adaptive feathering [11]) may limit their usefulness for design. The inclusion of a three-dimensional elastic shell model can afford an important understanding into the complex interaction between elastic, inertial, and aerodynamic forces/power [26], and how these relationships are shifted by tailoring the stiffness/mass throughout the shell. Such an insight should in turn lead to the development of efficient flapping wing designs for micro air vehicles.

Notwithstanding fluid–structure interactions and aeroelasticity, the mechanics of a nonlinear flapping shell are complex. The geometric nonlinearities should be able to accurately account for the large displacements (on the order of the wing length) and rotations ($\sim 90°$) commonly seen in natural flyers [6,11]. The large rigid body flapping motions qualify as a flexible multibody dynamics problem [28], with inherent coupling between the nonlinear elastic motion and the prescribed rigid body motion (Coriolis forces, e.g.). General studies pertaining to nonlinear shell models subjected to large overall motions are given by Madenci and Barut [17] and Yoo and Chung [29]; work specifically dealing with flapping wing shells (subjected to inertial loads) is given by Combes and Daniel [3] and Stanford and Beran [22].

The inclusion of aerodynamic as well as inertial loading necessitates a fluid–structure interaction study, increasing the computational cost substantially. For an implicit analysis, a sub-iteration loop is required within each time step to bring the shell motion into equilibrium with the surrounding fluid motion, by passing pressures and surface displacements/velocities between the two solvers (via various interpolation techniques) until convergence. Aeroelastic analysis of a flapping shell has been studied by several authors, with varying degrees of aerodynamic modeling fidelity: Singh and Chopra [20] (blade element aerodynamics), Zhu [31] and Stanford and Beran [23] (vortex lattice aerodynamics), Hamamoto et al. [9], Chimakurthi et al. [2], Luo et al. [16] (Navier–Stokes aerodynamics).

It is the goal of this work to determine the thrust- and power-optimal stiffness and mass distributions throughout an aeroelastic flapping shell in forward flight. Previous work in this area is relatively rare: the optimal thickness distribution of a flapping beam is considered by Isogai and Harino [12], Stanford et al. [24], and Thomson [27]. Ho et al. [11] discuss the optimal stiffness distribution (by controlling the elastic modulus at different patches along the wing) of a flapping shell. The work presented below adopts the thickness of each shell finite element along the wing as a design variable; which will explicitly control the local mass and stiffness, and implicitly affect the resulting aerodynamic forces of the coupled system. The number of design variables is then proportional to the grid density; a certain level of fineness is required for accuracy, but also in order to emulate the detailed topological features seen in many biological flyers [3].

* Corresponding author.
E-mail address: bret.stanford@wpafb.af.mil (B. Stanford).

1270-9638/$ – see front matter Published by Elsevier Masson SAS.
doi:10.1016/j.ast.2011.10.011

This article is a U.S. government work, and is not subject to copyright in the United States.

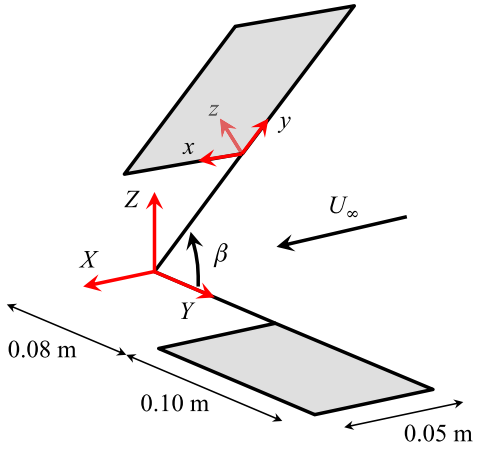

Fig. 1. Flexible wing illustration and coordinate system definition.

Few options exist for optimization with a large number of design variables other than gradient-based methods, where the design derivatives are computed in an analytical manner. These methods can use either direct or adjoint techniques. The former directly computes the derivative of the system response with respect to the design variables via a linear system of equations with multiple right-hand sides (one per design variable). This linear set of equations can be integrated forward in time, along with the nonlinear set of aeroelastic equations [24]. Conversely, the adjoint method requires the solution of a linear set of equations with multiple right-hand sides (one per constraint, and thus independent of the number of design variables [8]. This equation must be integrated in reverse time: the system response and the adjoint cannot be computed simultaneously, and the storage costs can be large [14]. It is expected that, for the aeroelastic model considered here, the direct method should be simpler to implement, less computationally intensive, and require less storage space [23].

The remainder of this work is organized as follows: first, the aeroelastic framework and the concomitant sensitivity analysis are formulated in detail. The parameters that define the flapping problem are then provided, followed by a brief discussion into the salient features of the baseline aeroelastic behavior. Thrust and efficiency design gradients (with respect to the thickness of each finite element) are given for a variety of shell boundary conditions. The work concludes with the thrust- and power-optimal thickness distributions for each case, and the important aeroelastic features thought to be responsible for the beneficial tailoring.

2. Aeroelastic modeling

An illustration of the problem definition considered here can be found in Fig. 1. There exists a fixed inertial coordinate system (XYZ) as well as a moving coordinate system (xyz) attached to the root of a flexible rectangular wing. The wing length is 0.1 m, the wing chord is 0.05 m, and the wing is offset from the origin of the inertial coordinate system by 0.08 m. The flow velocity U_∞ is along the X-axis, and the wing flaps about this axis as well, with the kinematics described by a single Euler angle β. Aeroelastic behavior is assumed to be symmetric across the XZ plane: i.e., a pair wing (not shown) exists in the $-XY$ plane.

The structural model used in this work is a nonlinear shell model computed via a corotational approximation of the updated Lagrangian approach [17]. The wing structure is discretized into triangular finite elements, with 6 degrees of freedom (three displacements and three rotations) per node. The equations of motion at time step i are:

$$\boldsymbol{M}\cdot\ddot{\boldsymbol{u}}^i+\boldsymbol{C}\cdot\dot{\boldsymbol{u}}^i+\boldsymbol{P}^i=\boldsymbol{F}^i \tag{1}$$

where $\boldsymbol{u}^i$ is the solution vector measured in the body-attached coordinate system, along with this first two time derivatives. The consistent mass matrix $\boldsymbol{M}$ and the structural damping matrix $\boldsymbol{C}$ (indicative of the energy dissipated by the vibrating structure) are constant entities, and have no time step superscript. $\boldsymbol{F}^i$ is a vector of external forces composed of both inertial (due to the rigid body motion) and aerodynamic forces. $\boldsymbol{P}^i$ is a vector of internal forces, a nonlinear function of the shell deformation. The tangent stiffness matrix is computed analytically as:

$$\boldsymbol{K}^i=\frac{\partial\boldsymbol{P}^i}{\partial\boldsymbol{u}^i} \tag{2}$$

The stiffness matrix contains in-plane membrane terms (modeled with an LST element), out-of-plane bending terms (modeled with a DKT element), nonlinear stress stiffening, and spin-softening terms (representing a coupling between elastic deformation and rigid body rotations of the body-attached coordinate system) [5]. Eq. (1) is integrated with a generalized-α method [15], using the tangent stiffness matrix to drive the residual below a specified tolerance at each time step via the Newton–Raphson method. Time derivatives are approximated with standard Newmark terms. Further information concerning the nonlinear shell dynamics model, as well as verification studies, can be found in Ref. [22].

Having solved Eq. (1), the shape of the wing, again measured in the body-attached coordinate system, is updated:

$$\boldsymbol{z}^i=\boldsymbol{z}_o+\boldsymbol{Q}\cdot\boldsymbol{u}^i \tag{3}$$

$\boldsymbol{z}^i$ is a vector which contains the x, y, and z coordinates of each node along the wing, $\boldsymbol{z}_o$ is the shape of the undeformed wing (Fig. 1), and $\boldsymbol{Q}$ is an interpolation matrix. The deformation vector $\boldsymbol{u}^i$ contains displacements and rotations of each free finite element node: $\boldsymbol{Q}$ removes the rotations and adds back in the displacements of the fixed (i.e., clamped) nodes, which are zero.

The unsteady vortex lattice solver proceeds as follows [13]: the shape of the wing at time step i is first defined by Eq. (3). This geometry is then transformed into the inertial coordinate system, where the wing is discretized into a lattice of vortex ring singularities, with a collocation point located at the center of each. The vortex rings along the trailing edge of the wing are convected into the wake, while the strength (circulation) of each of these rings is set equal to that computed at the previous time step, and held fixed. A system of equations is developed and solved for the new circulation distribution throughout the wing: velocities due to wing–wing interactions, wake–wing interactions, free-stream velocities, wing rotations/translations, and wing deformation must all cancel each other in the direction normal to each collocation point. This stipulates that the wing becomes a stream-surface of the flow:

$$\boldsymbol{C}_1^i\cdot\boldsymbol{\Gamma}^i+\boldsymbol{C}_2^i\cdot\boldsymbol{\Gamma}_w^i=\boldsymbol{L}^i \tag{4}$$

where $\boldsymbol{C}_1^i$ and $\boldsymbol{C}_2^i$ are wing–wing and wake–wing influence matrices (as computed with the Biot–Savart law). The source vector $\boldsymbol{L}^i$ is the velocity along the outward normal of each collocation point due to the wing movement, $\boldsymbol{\Gamma}_w^i$ is the strength of the wake, and $\boldsymbol{\Gamma}^i$ is the unknown strength of the wing, which is computed by inverting the wing–wing influence matrix. The local streamline at each wake ring can be computed through the wing–wake and wake–wake interactions, and subsequently deformed [21].

The wing-circulation distribution can be used to compute the induced velocity at each collocation point (for induced drag computations):

$$\boldsymbol{w}^i=\boldsymbol{C}_{w1}^i\cdot\boldsymbol{\Gamma}^i+\boldsymbol{C}_{w2}^i\cdot\boldsymbol{\Gamma}_w^i \tag{5}$$

These influence matrices are similar to those found in Eq. (4), but only include the streamwise portions of each vortex ring [13]. The

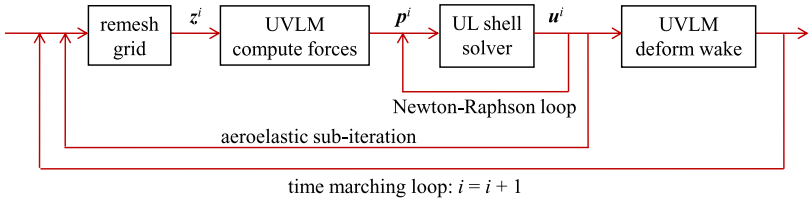

Fig. 2. Implicit aeroelastic coupling loop.

velocity for these terms is not resolved along the outward normal of each panel, but along the local lift vector of each panel (perpendicular to the flow). The pressures $\boldsymbol{p}^i$ and integrated forces (lift, thrust, etc.) can be subsequently computed as well.

Aeroelastic coupling is performed with an implicit time marching scheme via a fluid–structure sub-iteration loop within each time step, as seen in Fig. 2. Within an aeroelastic sub-iteration, the wing grid is meshed via Eq. (3). The geometry information is used to compute the pressure distribution $\boldsymbol{p}^i$ over the wing via the unsteady vortex lattice method. This pressure distribution, along with known values of the structural deformation, velocity, acceleration, external forces, and internal forces from the previous $i-1$ time step, are used within a Newton–Raphson update loop to compute the deformation at the current step i (Eq. (1)). The iterations commence within the updated Lagrangian loop until the residual is driven below a specified tolerance. The aeroelastic sub-iterations commence until an aeroelastic residual (defined here as the norm of the difference in the pressure vector computed at consecutive sub-iterations) is driven below a specified tolerance. Having converged, the vortex lattice method can be used to find the new shape of the wake, and the time step counter is increased to $i+1$.

Validation of the resulting aeroelastic framework is provided in Ref. [23], via comparison with the experimental data of Heathcote et al. [10] for a plunging elastic plate in a water tunnel.

3. Aeroelastic sensitivity analysis

For this work, it is assumed that an optimization framework will contain objective functions and constraints formulated as time-averaged quantities:

$$g = \int_{t_o}^{t_f} G \cdot dt \sim \sum_{i=I_o}^{I_f} \omega^i \cdot G^i \tag{6}$$

where G^i is a scalar property of the aeroelastic deformation at time step i. It is desired to numerically integrate over a certain time period of interest (assumed to lie between time steps I_o and I_f), where ω^i are weighting coefficients. For this work, G^i is an aerodynamic force-based quantity, generically written as:

$$G^i = f\left(\boldsymbol{z}^i, \boldsymbol{z}^{i-1}, \boldsymbol{w}^i, \boldsymbol{\Gamma}^i, \boldsymbol{\Gamma}^{i-1}\right) \tag{7}$$

All time derivatives (wing velocities for the source vector $\boldsymbol{L}^i$, as well as $d\boldsymbol{\Gamma}^i/dt$ terms for the unsteady Bernoulli equation [13]) are computed with a backward finite difference equation, so information is needed at the previous time step to compute forces within the current time step.

The design variables are given by $\boldsymbol{x}$, which for this work will be a large vector containing structural parameters. Specifically, the thickness of each finite element is used, but any structural sizing variable could be used in the formulation given below. For gradient-based optimization, the derivative of the scalar objective/constraint with respect to $\boldsymbol{x}$ is needed:

$$\frac{dg}{d\boldsymbol{x}} = \sum_{i=I_o}^{I_f} \omega_i \cdot \frac{dG^i}{d\boldsymbol{x}} \tag{8}$$

This derivative can be computed with the chain rule, via the five dependencies listed in Eq. (7):

$$\begin{aligned}\frac{dG^i}{d\boldsymbol{x}} = {} & \frac{\partial G^i}{\partial \boldsymbol{z}^i} \cdot \boldsymbol{Q} \cdot \frac{d\boldsymbol{u}^i}{d\boldsymbol{x}} + \frac{\partial G^i}{\partial \boldsymbol{z}^{i-1}} \cdot \boldsymbol{Q} \cdot \frac{d\boldsymbol{u}^{i-1}}{d\boldsymbol{x}} + \frac{\partial G^i}{\partial \boldsymbol{w}^i} \cdot \frac{d\boldsymbol{w}^i}{d\boldsymbol{x}} \\ & + \frac{\partial G^i}{\partial \boldsymbol{\Gamma}^i} \cdot \frac{d\boldsymbol{\Gamma}^i}{d\boldsymbol{x}} + \frac{\partial G^i}{\partial \boldsymbol{\Gamma}^{i-1}} \cdot \frac{d\boldsymbol{\Gamma}^{i-1}}{d\boldsymbol{x}}\end{aligned} \tag{9}$$

The first terms in the five products in Eq. (9) can be computed directly, as G^i is a known function of these vectors; the remaining terms (essentially the derivative of the aeroelastic system response) require additional effort.

From the structural model, the following dependencies are observed:

$$\begin{aligned}&\boldsymbol{M} = f(\boldsymbol{x}), \qquad \boldsymbol{C} = f(\boldsymbol{x}), \qquad \boldsymbol{P}^i = f\left(\boldsymbol{x}, \boldsymbol{u}^i\right) \\ &\boldsymbol{F}^i = f\left(\boldsymbol{x}, \boldsymbol{u}^i, \boldsymbol{p}^i\right)\end{aligned} \tag{10}$$

The mass and damping matrices are only functions of $\boldsymbol{x}$, while the internal force vector depends (nonlinearly) upon the solution vector $\boldsymbol{u}^i$ as well (Eq. (2)). The external force vector depends upon $\boldsymbol{x}$ (in the case of large rigid body motions, heavier wing structures have stronger inertial forces), the pressure $\boldsymbol{p}^i$, and the deformation $\boldsymbol{u}^i$. The pressure loads are typically nonconservative follower forces: wing deformation changes the direction of the loads, hence the last dependency. The derivative of the finite element analysis (Eq. (1)) is:

$$\frac{d\boldsymbol{M}}{d\boldsymbol{x}} \cdot \ddot{\boldsymbol{u}}^i + \boldsymbol{M} \cdot \frac{d\ddot{\boldsymbol{u}}^i}{d\boldsymbol{x}} + \frac{d\boldsymbol{C}}{d\boldsymbol{x}} \cdot \dot{\boldsymbol{u}}^i + \boldsymbol{C} \cdot \frac{d\dot{\boldsymbol{u}}^i}{d\boldsymbol{x}} + \boldsymbol{K}^i \cdot \frac{d\boldsymbol{u}^i}{d\boldsymbol{x}} + \frac{\partial \boldsymbol{P}^i}{\partial \boldsymbol{x}} = \frac{d\boldsymbol{F}^i}{d\boldsymbol{x}} \tag{11}$$

where the derivatives of the mass and damping matrices are known triply-indexed terms [22]. The derivative of the force vector can be expanded based upon the three dependencies of Eq. (10):

$$\frac{d\boldsymbol{F}^i}{d\boldsymbol{x}} = \frac{\partial \boldsymbol{F}^i}{\partial \boldsymbol{x}} + \frac{\partial \boldsymbol{F}^i}{\partial \boldsymbol{p}^i} \cdot \frac{d\boldsymbol{p}^i}{d\boldsymbol{x}} + \frac{\partial \boldsymbol{F}^i}{\partial \boldsymbol{u}^i} \cdot \frac{d\boldsymbol{u}^i}{d\boldsymbol{x}} \tag{12}$$

The first term is an explicit dependence upon $\boldsymbol{x}$ (typically via the inertial forces), whereas the latter two products are implicit dependencies through the pressure and structural deformation. The dependence of the force on the pressure is easily computed, while the dependence upon the deformation (due to the nonconservative pressure loads) is the skew-symmetric external stiffness matrix [5]:

$$\frac{\partial \boldsymbol{F}^i}{\partial \boldsymbol{u}^i} = \boldsymbol{K}^i_{ext} \tag{13}$$

Similar to Eq. (7), the aerodynamic pressures depend upon the wing geometry and circulation at the current and previous time step (due to the finite differences used for the unsteady Bernoulli equation):

$$\boldsymbol{p}^i = f\left(\boldsymbol{z}^i, \boldsymbol{z}^{i-1}, \boldsymbol{\Gamma}^i, \boldsymbol{\Gamma}^{i-1}\right) \tag{14}$$

As above, the derivative can be expanded through the chain rule:

$$\frac{d\boldsymbol{p}^i}{d\boldsymbol{x}} = \frac{\partial \boldsymbol{p}^i}{\partial \boldsymbol{z}^i}\cdot\boldsymbol{Q}\cdot\frac{d\boldsymbol{u}^i}{d\boldsymbol{x}} + \frac{\partial \boldsymbol{p}^i}{\partial \boldsymbol{z}^{i-1}}\cdot\boldsymbol{Q}\cdot\frac{d\boldsymbol{u}^{i-1}}{d\boldsymbol{x}} + \frac{\partial \boldsymbol{p}^i}{\partial \boldsymbol{\Gamma}^i}\cdot\frac{d\boldsymbol{\Gamma}^i}{d\boldsymbol{x}} + \frac{\partial \boldsymbol{p}^i}{\partial \boldsymbol{\Gamma}^{i-1}}\cdot\frac{d\boldsymbol{\Gamma}^{i-1}}{d\boldsymbol{x}} \tag{15}$$

The derivative of the wing circulation with respect to $\boldsymbol{x}$ requires a differentiation of the unsteady vortex lattice method. The following dependencies are observed:

$$\boldsymbol{C}_1^i = f\left(\boldsymbol{z}^i\right), \qquad \boldsymbol{C}_2^i = f\left(\boldsymbol{z}^i, \boldsymbol{z}^{i-1}, \ldots, \boldsymbol{z}^1\right)$$
$$\boldsymbol{L}^i = f\left(\boldsymbol{z}^i, \boldsymbol{z}^{i-1}\right) \tag{16}$$

The wing–wing influence matrix is only a function of the wing geometry at the current time step (as computed with the Biot–Savart law). The wake–wing influence matrix is a function of the current wing geometry and the current wake geometry. The wake geometry, however, is a function of the previous wake and wing geometry: a recursive relationship exists back to the initial time step. The end result is that $\boldsymbol{C}_2^i$ is a function of the wing geometry at every preceding time step. The source vector $\boldsymbol{L}^i$ contains wing velocity terms, which are computed with finite differences. As such, the geometry at both the current and the previous time steps are required. Similar dependencies can be written for the influence matrices of Eq. (5):

$$\boldsymbol{C}_{w1}^i = f\left(\boldsymbol{z}^i, \boldsymbol{z}^{i-1}\right), \qquad \boldsymbol{C}_{w2}^i = f\left(\boldsymbol{z}^i, \boldsymbol{z}^{i-1}, \ldots, \boldsymbol{z}^1\right) \tag{17}$$

As can be inferred from Eq. (4) and Eq. (16), the wing circulation $\boldsymbol{\Gamma}^i$ is an explicit function of the wing geometry at every time step between 1 and i, while the wake circulation $\boldsymbol{\Gamma}_w^i$ depends upon geometry up to time step $i-1$:

$$\boldsymbol{\Gamma}^i = f\left(\boldsymbol{z}^i, \boldsymbol{z}^{i-1}, \ldots, \boldsymbol{z}^1\right), \qquad \boldsymbol{\Gamma}_w^i = f\left(\boldsymbol{z}^{i-1}, \boldsymbol{z}^{i-2}, \ldots, \boldsymbol{z}^1\right) \tag{18}$$

The circulation derivatives needed in Eq. (15) can thus be computed with a chain rule, summing terms from the initial step to the current step i:

$$\frac{d\boldsymbol{\Gamma}^i}{d\boldsymbol{x}} = \sum_{j=1}^{i}\left(\frac{\partial \boldsymbol{\Gamma}^i}{\partial \boldsymbol{z}^j}\cdot\boldsymbol{Q}\cdot\frac{d\boldsymbol{u}^j}{d\boldsymbol{x}}\right) \tag{19}$$

The sensitivities $\partial\boldsymbol{\Gamma}^i/\partial\boldsymbol{z}^j$ are computed by differentiating the no-penetration condition (Eq. (4)):

$$\boldsymbol{C}_1^i\cdot\frac{\partial \boldsymbol{\Gamma}^i}{\partial \boldsymbol{z}^j} = \begin{cases} \frac{\partial \boldsymbol{L}^i}{\partial \boldsymbol{z}^i} - \frac{\partial \boldsymbol{C}_1^i}{\partial \boldsymbol{z}^i}\cdot\boldsymbol{\Gamma}^i - \frac{\partial \boldsymbol{C}_2^i}{\partial \boldsymbol{z}^i}\cdot\boldsymbol{\Gamma}_w^i, & j = i \\ \frac{\partial \boldsymbol{L}^i}{\partial \boldsymbol{z}^{i-1}} - \frac{\partial \boldsymbol{C}_2^i}{\partial \boldsymbol{z}^{i-1}}\cdot\boldsymbol{\Gamma}_w^i - \boldsymbol{C}_2^i\cdot\frac{\partial \boldsymbol{\Gamma}_w^i}{\partial \boldsymbol{z}^{i-1}}, & j = i-1 \\ -\frac{\partial \boldsymbol{C}_2^i}{\partial \boldsymbol{z}^j}\cdot\boldsymbol{\Gamma}_w^i - \boldsymbol{C}_2^i\cdot\frac{\partial \boldsymbol{\Gamma}_w^i}{\partial \boldsymbol{z}^j}, & j < i-1 \end{cases} \tag{20}$$

A piecewise expression is required because $\boldsymbol{L}^i$ is only a function of $\boldsymbol{z}^i$ and $\boldsymbol{z}^{i-1}$ (Eq. (16)), and the wake circulation at step i is not a function of the geometry at step i. Derivatives of the influence matrices are triply-indexed terms, computed by differentiating the Biot–Savart law. Derivatives of the wake terms (as well as the sensitivity of $\boldsymbol{C}_2^i$ upon the geometry at previous time steps) require differentiating the wake shedding and updating algorithms, as these terms provide the only connection between the forces generated at disparate time steps. Further information can be found in Ref. [21].

Each of the piecewise expressions requires the solution to a system of equations with multiple right-hand sides (equal to the size of $\boldsymbol{z}^i$, or three times the number of nodes), a hallmark of the direct method of analytical differentiation of discrete systems. As the influence matrix will not be particularly large, the computational cost of such an endeavor will grow slowly with the mesh density. Eq. (19) can then be inserted into Eq. (15), and like-terms grouped together (which involves removing the last two terms from the summation of Eq. (19):

$$\frac{d\boldsymbol{p}^i}{d\boldsymbol{x}} = \left(\frac{\partial \boldsymbol{p}^i}{\partial \boldsymbol{\Gamma}^i}\cdot\frac{\partial \boldsymbol{\Gamma}^i}{\partial \boldsymbol{z}^i} + \frac{\partial \boldsymbol{p}^i}{\partial \boldsymbol{z}^i}\right)\cdot\boldsymbol{Q}\cdot\frac{d\boldsymbol{u}^i}{d\boldsymbol{x}} + \left(\frac{\partial \boldsymbol{p}^i}{\partial \boldsymbol{\Gamma}^i}\cdot\frac{\partial \boldsymbol{\Gamma}^i}{\partial \boldsymbol{z}^{i-1}} + \frac{\partial \boldsymbol{p}^i}{\partial \boldsymbol{z}^{i-1}}\right)\cdot\boldsymbol{Q}\cdot\frac{d\boldsymbol{u}^{i-1}}{d\boldsymbol{x}} + \frac{\partial \boldsymbol{p}^i}{\partial \boldsymbol{\Gamma}^i}\cdot\sum_{j=1}^{i-2}\left(\frac{\partial \boldsymbol{\Gamma}^i}{\partial \boldsymbol{z}^j}\cdot\boldsymbol{Q}\cdot\frac{d\boldsymbol{u}^j}{d\boldsymbol{x}}\right) + \frac{\partial \boldsymbol{p}^i}{\partial \boldsymbol{\Gamma}^{i-1}}\cdot\frac{d\boldsymbol{\Gamma}^{i-1}}{d\boldsymbol{x}} \tag{21}$$

Eq. (21) can then be inserted into Eq. (12), which in turn can be inserted into Eq. (11). Terms containing $d\boldsymbol{u}^i/d\boldsymbol{x}$, as well as its time-derivatives are brought to the right side of Eq. (11), while the remainder of the terms are brought to the left side. Eq. (11) can then be re-written as:

$$\begin{aligned} \boldsymbol{M}\cdot\frac{d\ddot{\boldsymbol{u}}^i}{d\boldsymbol{x}} + \boldsymbol{C}\cdot\frac{d\dot{\boldsymbol{u}}^i}{d\boldsymbol{x}} + \left(\boldsymbol{K}^i - \boldsymbol{K}_{ext}^i - \frac{\partial \boldsymbol{F}^i}{\partial \boldsymbol{p}^i}\cdot\left(\frac{\partial \boldsymbol{p}^i}{\partial \boldsymbol{\Gamma}^i}\cdot\frac{\partial \boldsymbol{\Gamma}^i}{\partial \boldsymbol{z}^i} + \frac{\partial \boldsymbol{p}^i}{\partial \boldsymbol{z}^i}\right)\cdot\boldsymbol{Q}\right)\cdot\frac{d\boldsymbol{u}^i}{d\boldsymbol{x}} \\ = \frac{\partial \boldsymbol{F}^i}{\partial \boldsymbol{x}} - \frac{d\boldsymbol{M}}{d\boldsymbol{x}}\cdot\ddot{\boldsymbol{u}}^i - \frac{d\boldsymbol{C}}{d\boldsymbol{x}}\cdot\dot{\boldsymbol{u}}^i - \frac{\partial \boldsymbol{P}^i}{\partial \boldsymbol{x}} \\ + \frac{\partial \boldsymbol{F}^i}{\partial \boldsymbol{p}^i}\cdot\left(\frac{\partial \boldsymbol{p}^i}{\partial \boldsymbol{\Gamma}^i}\cdot\frac{\partial \boldsymbol{\Gamma}^i}{\partial \boldsymbol{z}^{i-1}} + \frac{\partial \boldsymbol{p}^i}{\partial \boldsymbol{z}^{i-1}}\right)\cdot\boldsymbol{Q}\cdot\frac{d\boldsymbol{u}^{i-1}}{d\boldsymbol{x}} \\ + \frac{\partial \boldsymbol{F}^i}{\partial \boldsymbol{p}^i}\cdot\frac{\partial \boldsymbol{p}^i}{\partial \boldsymbol{\Gamma}^i}\cdot\sum_{j=1}^{i-2}\left(\frac{\partial \boldsymbol{\Gamma}^i}{\partial \boldsymbol{z}^j}\cdot\boldsymbol{Q}\cdot\frac{d\boldsymbol{u}^j}{d\boldsymbol{x}}\right) \\ + \frac{\partial \boldsymbol{F}^i}{\partial \boldsymbol{p}^i}\cdot\frac{\partial \boldsymbol{p}^i}{\partial \boldsymbol{\Gamma}^{i-1}}\cdot\frac{d\boldsymbol{\Gamma}^{i-1}}{d\boldsymbol{x}} \end{aligned} \tag{22}$$

Eq. (22) represents a second equation that must be solved at each time step in conjunction with Eq. (1), to compute $d\boldsymbol{u}^i/d\boldsymbol{x}$ as it evolves with time. At time step i, every term on the right side of Eq. (22) is known: $d\boldsymbol{u}^j/d\boldsymbol{x}$ is known from the previous j time steps, as is $d\boldsymbol{\Gamma}^{i-1}/d\boldsymbol{x}$ (Eq. (19)). Furthermore, the time derivatives of $\boldsymbol{u}^i$ will also be known, as Eq. (1) must be solved at the time step i step before Eq. (22) can be. Eq. (22) can be written compactly as:

$$\boldsymbol{M}\cdot\frac{d\ddot{\boldsymbol{u}}^i}{d\boldsymbol{x}} + \boldsymbol{C}\cdot\frac{d\dot{\boldsymbol{u}}^i}{d\boldsymbol{x}} + \boldsymbol{K}_{sa}^i\cdot\frac{d\boldsymbol{u}^i}{d\boldsymbol{x}} = \boldsymbol{F}_{sa}^i \tag{23}$$

Eq. (23) is a linear set of differential equations with time-dependent coefficients ($\boldsymbol{K}_{sa}^i$ is defined a priori at each time step, and does not depend upon $d\boldsymbol{u}^i/d\boldsymbol{x}$) and multiple right-hand sides, due, as before, to the use of the direct method of differentiation. $\boldsymbol{F}_{sa}^i$ and $d\boldsymbol{u}^i/d\boldsymbol{x}$ (as well as the latter's time derivatives) are matrices of size $N_{DOF}\times N_{DV}$, where the former is the number of free degrees of freedom in the finite element method, and the latter is the number of design variables (length of $\boldsymbol{x}$). As with the system response, Eq. (23) is integrated with a generalized-α method, using Newmark terms to approximate the time derivatives.

The derivative of the induced velocity is also needed in Eq. (9). As with the circulation, the downwash at time step i is an explicit function of the wing geometry at every previous time step:

$$\frac{d\boldsymbol{w}^i}{d\boldsymbol{x}} = \sum_{j=1}^{i}\left(\frac{\partial \boldsymbol{w}^i}{\partial \boldsymbol{z}^j}\cdot\boldsymbol{Q}\cdot\frac{d\boldsymbol{u}^j}{d\boldsymbol{x}}\right) \tag{24}$$

The derivative of the induced velocity with the respect to the wing shape is computed in a similar manner to Eq. (20), with a piecewise expression:

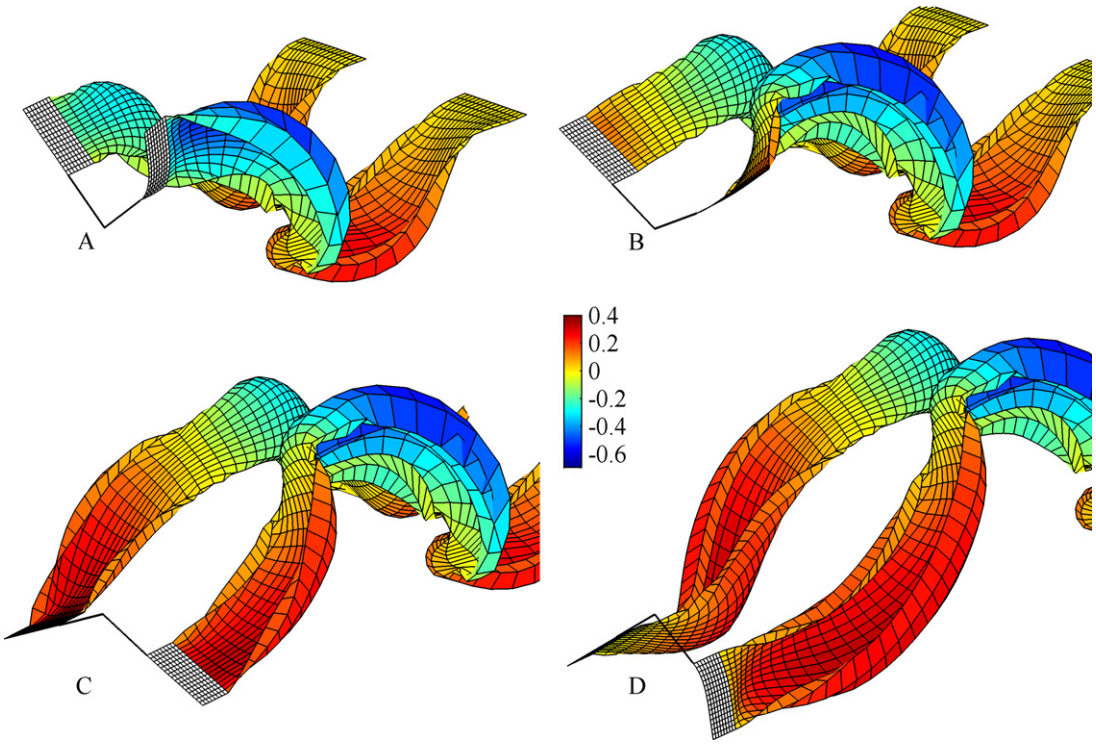

Fig. 3. Wing and wake shapes at four instants in time throughout the downstroke: rigid wing (left), flexible wing (right). Contour plot denotes wake strength ($\boldsymbol{\Gamma}_w$).

$$\frac{\partial \boldsymbol{w}^i}{\partial \boldsymbol{z}^j} = \begin{cases} \frac{\partial \boldsymbol{C}^i_{w1}}{\partial \boldsymbol{z}^i} \cdot \boldsymbol{\Gamma}^i + \boldsymbol{C}^i_{w1} \cdot \frac{\partial \boldsymbol{\Gamma}^i}{\partial \boldsymbol{z}^i} + \frac{\partial \boldsymbol{C}^i_{w2}}{\partial \boldsymbol{z}^i} \cdot \boldsymbol{\Gamma}^i_w, & j = i \\ \frac{\partial \boldsymbol{C}^i_{w1}}{\partial \boldsymbol{z}^{i-1}} \cdot \boldsymbol{\Gamma}^i + \boldsymbol{C}^i_{w1} \cdot \frac{\partial \boldsymbol{\Gamma}^i}{\partial \boldsymbol{z}^{i-1}} + \frac{\partial \boldsymbol{C}^i_{w2}}{\partial \boldsymbol{z}^{i-1}} \cdot \boldsymbol{\Gamma}^i_w \\ \quad + \boldsymbol{C}^i_{w2} \cdot \frac{\partial \boldsymbol{\Gamma}^i_w}{\partial \boldsymbol{z}^{i-1}}, \quad j = i-1 \\ \boldsymbol{C}^i_{w1} \cdot \frac{\partial \boldsymbol{\Gamma}^i}{\partial \boldsymbol{z}^j} + \frac{\partial \boldsymbol{C}^i_{w2}}{\partial \boldsymbol{z}^j} \cdot \boldsymbol{\Gamma}^i_w + \boldsymbol{C}^i_{w2} \cdot \frac{\partial \boldsymbol{\Gamma}^i_w}{\partial \boldsymbol{z}^j}, & j < i-1 \end{cases} \tag{25}$$

Having solved Eq. (23) at a given time step, the relevant terms can be inserted into Eq. (24), and everything needed to evaluate $dG^i/d\boldsymbol{x}$ in Eq. (9) is then available. Integration of both the system response (Eq. (1)) and the sensitivity analysis (Eq. (23)) proceeds through time step I_f, at which point $dg/d\boldsymbol{x}$ of Eq. (8) can be evaluated.

Verification of the aeroelastic sensitivities is provided in Ref. [23], via comparison with finite difference approximations.

4. Flapping wing description

The flapping wing considered in this work is shown graphically in Fig. 1; the flapping motion is given by:

$$\beta = \beta_m \cdot \left(1 - e^{\beta_o \cdot t^2}\right) \cdot \sin(\omega \cdot t) \tag{26}$$

where an exponentially-decaying start-up motion is included to facilitate convergence of the nonlinear system (Eq. (1)). Further parameters governing the aeroelastic system are given in Table 1: the fluid medium is air, the plate's material properties are estimated from that of carbon fiber composites (though the plate is modeled as isotropic for this work), and the structural damping matrix $\boldsymbol{C}$ is given as proportional to the mass matrix (Rayleigh damping [5]). The thickness value given in Table 1 is a baseline value, more details are found below. The resulting Reynolds number ($Re = \rho_\infty \cdot U_\infty \cdot c/\mu$) is 17,000 and the reduced frequency ($k = \omega \cdot c/2/U_\infty$) is 0.2.

The same wing mesh is used for both the structural shell model and the unsteady vortex lattice method. The latter discretizes the wing into quadrilateral rings, each of which is divided into two triangular shell elements for the structural solver. The wing is discretized into 16 panels along the wing length and 8 chordwise panels, providing 128 vortex rings for the aerodynamic solver and 256 triangular elements for the structural solver. Each flapping cycle is divided into 50 time steps, and 4 cycles are found to be sufficient for the aeroelastic response to set up into a periodic state. For both the aeroelastic sub-iteration loop and the updated Lagrangian loop shown in Fig. 2, the specified tolerance on the norm of the residual vectors is 10^{-6}, and both loops typically converge in less than 5 iterations.

Table 1
System parameters for aeroelastic simulation.

Chord, c	0.05 m	Elastic modulus, E	40 GPa
Wing length, l	0.10 m	Poisson's ratio, ν	0.3
Flow velocity, U_∞	5 m/s	Plate density, ρ_{wing}	1400 kg/m^3
Flow density, ρ_∞	1.225 kg/m^3	Plate thickness, t_{wing}	0.5 mm
β_m	$-\pi/4$	Plate damping, $\boldsymbol{C}$	$20 \cdot \boldsymbol{M}$
β_o	-1000	Frequency, ω	40 rad/s

5. Aeroelastic response and derivatives

Typical wing shapes and wake structures are given in Fig. 3 for four snapshots in time during the downstroke of the second flapping cycle. The contour levels given throughout the wake indicate the circulation ($\boldsymbol{\Gamma}_w$), where the circulation of each wake ring is held fixed throughout the simulation (no decay). Two cases are shown in Fig. 3: a rigid wing is given on the left of each plot, and a flexible wing on the right. This is only done to provide a direct qualitative visual comparison, as the two cases were originally run separately with symmetry assumed about the X–Z plane. In either case, the deformation of the wake is substantial, with strong tip vortices shed from the in-board and out-board (wingtip) of each wing. Only the newest 10 rings shed from the trailing edge are deformed, the remainder of the wake is merely convected downstream by U_∞. Relaxing this assumption would lead to more chaotic features in the older portions of the wake and also produce

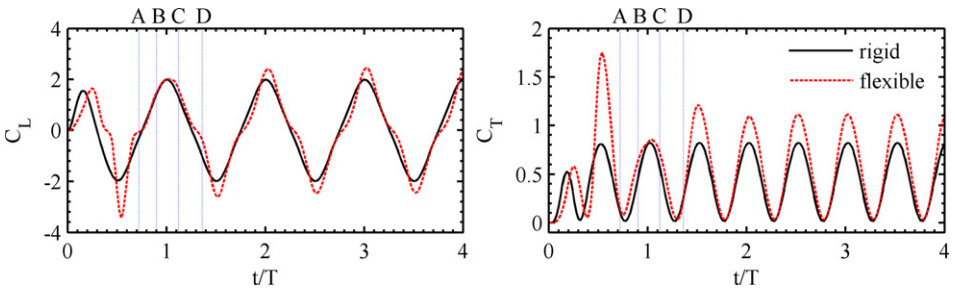

Fig. 4. Lift and thrust histories, with four specified instances in time corresponding to Fig. 3.

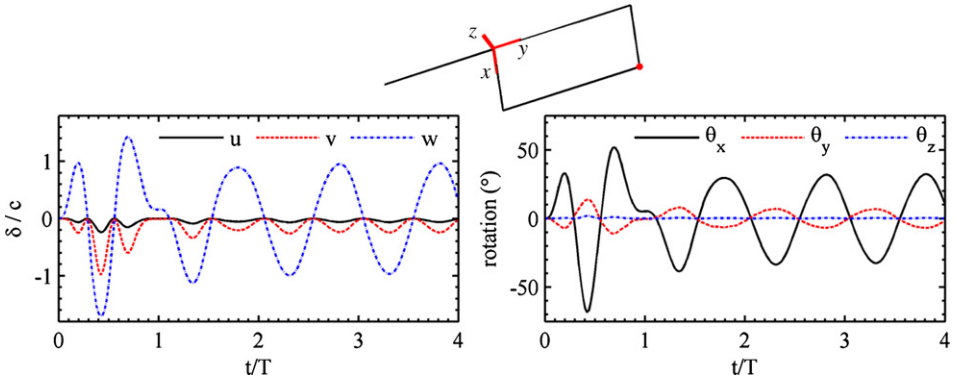

Fig. 5. Deformational displacement and rotation at the trailing edge wingtip, as measured in the body-attached coordinate system, corresponding to the flapping motion of Fig. 3.

well-defined reverse Kármán vortex streets (as the motion seen in Fig. 3 is thrust-producing). The assumption should have a negligible effect upon the aerodynamic pressure distribution over the wing for the low reduced frequency considered here (0.2) however, and will provide substantial computational cost savings [7].

The flexible wing considered on the right side of the four snapshots has a thickness distribution which has been optimized for peak cycle-averaged thrust. Furthermore, any finite element node that lies along the in-board portion of the wing and is within a quarter-chord of the leading edge (referencing Fig. 1: $y = 0$, $x \leqslant c/4$) is considered to be clamped in the body-attached coordinate system. More details on both of these points are given below. It can be seen that the spanwise bending deformation of the wing is very large, with peak deflection at stroke-reversal. This deformational motion, superimposed upon the rigid body flapping motion (Eq. (26)), increases the velocity of the wing, and thus the wake circulation and concomitant tip vortex swirling, as compared to the rigid case.

The lift (positive in the Z direction) and thrust (positive in the $-X$ direction) coefficients corresponding to the data given in Fig. 3 are shown in Fig. 4 through four complete cycles. These coefficients, along with the power and the efficiency (used below), are defined as:

$$C_L = F_Z/\left(0.5 \cdot \rho_\infty \cdot U_\infty^2 \cdot c \cdot l\right)$$
$$C_T = -F_X/\left(0.5 \cdot \rho_\infty \cdot U_\infty^2 \cdot c \cdot l\right)$$
$$C_p = P/\left(0.5 \cdot \rho_\infty \cdot U_\infty^3 \cdot c \cdot l\right)$$
$$\eta = C_{T,ave}/C_{P,ave} \tag{27}$$

where F_X and F_Z are the aerodynamic forces in the corresponding directions, and P is the required power input. The exponential build-up of the flapping motions (via β_o) is clearly seen in the rigid thrust data of Fig. 4, completely decayed after the first cycle. Unsteady aerodynamic effects may also provide initial transients, but their influence should be small due to the low reduced frequency. Conversely, the initial transients in the flexible case are certainly due to unsteady aerostructural effects, and take roughly 2.5 cycles to decay, leaving a time-periodic motion. Damping is provided by both the aerodynamic loads, as well as the structural damping matrix $\boldsymbol{C}$.

Again focusing on the rigid data of Fig. 4, peak positive lift is found though the middle of the downstroke ($t/T = 1, 2, \ldots$) and peak negative lift through the middle of the upstroke ($t/T = 1.5, 2.5, \ldots$). Added mass effects can be expected to shift the phase between β and C_L [13] for higher reduced frequencies than considered here. Positive thrust is produced during both strokes, as the angle of attack induced by the flapping motion tilts the lift vector forward [19]. The induced drag computed by the vortex lattice method will oppose this thrust generation, but at no point in the flapping cycle is a total drag (negative thrust) produced. This is because (as specified by the kinematic motions) when the wing stops moving (and hence tilting of the lift vector is impossible), the physical angle of attack is zero, along with the induced drag.

The structural deformation at the trailing edge of the wingtip, as measured in the body-attached coordinate system, is given in Fig. 5. Despite the exponential build-up of the flapping motions, the initial displacements are very large, with out-of-plane displacements (w) approximately 1.7 chord lengths, or 85% of the wing length. This large initial deformation has a notable effect on the lift and thrust of Fig. 4, with peak thrust 60% larger than the eventual time-periodic amplitude. For the kinematics used here the inertial forces are entirely in phase with the flapping motion: peak positive force at the top of the upstroke ($t/T = 0.75, 1.75, \ldots$) and peak minimum force at the bottom of the downstroke ($t/T = 0.25, 1.25, \ldots$). The peak w-displacements (and corresponding θ_x) of Fig. 5 are largely due to these forces. A foreshortening of the wing (negative u-displacements) is also seen here, a hallmark of the geometrically nonlinear shell solution [29].

As the wing travels through the mid-stroke ($t/T = 0.5, 1, 1.5, \ldots$), the inertial forces, except for centripetal forces that act along the y-axis, are zero. The wing velocity is peak at these loca-

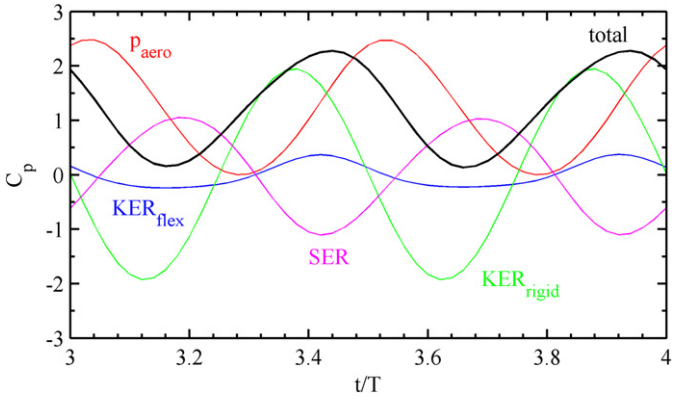

Fig. 6. Input power contributions corresponding to the flexible flapping motion of Fig. 3.

tions, and so deformation is largely due to aerodynamic forces. The retarding effect of the air leads to positive deflection through the downstroke, negative deflection through the upstroke. Based upon the relative magnitudes of the w-deflection at $t/T = 3.75$ (inertial force dominates) and 4 (aerodynamic force dominates), the former is roughly three times larger than the latter. It has been speculated [4] that, for some biological flyers, aerodynamic forces play a negligible role in the wing deformation; clearly for this case, such an assumption would be erroneous.

The increased lift and thrust of the flexible wing (as compared to the rigid wing, Fig. 4) occurs largely through the mid-stroke, and is due to the increased velocity of the wing [10] via the additive effect of $\dot{\beta}$ and $\dot{w}$. It is important to note that, for this case, the redistribution of aerodynamic pressure load due to the wing's substantial shape change (Fig. 3) is secondary; it is the deformational velocity which is the primary effect. An exception to this point is the wing torsion seen in Fig. 5 (θ_y). The topological details of the wing structure (discussed below) provide the wing with a negative bend–twist coupling (i.e., adaptive feathering [21]). This change in angle of attack shifts the lift coefficient of the flexible wing at stroke reversal, when the bending (and hence the torsion) is peak.

The required input power coefficient of the flexible wing is given in Fig. 6 for the final (time periodic) flapping motion. The total power requirement is computed via a sum of the aerodynamic power, the strain energy rate (*SER*), and the kinetic energy rate (*KER*). The kinetic energy rate is further broken into rigid and deformational contributions. The aerodynamic power is largely positive (i.e., work is always expended to move the wing through the fluid), but the remaining terms have positive and negative contributions. This is as expected: for the elastic term, energy is continually stored and converted as the beam vibrates. For the rigid term, work is expended to accelerate the wing, and a nearly equal amount is released during the deceleration. Following the terminology of Tantanawat and Kota [26] the flow of energy between the aerodynamic power and the elastic terms is "generative load exploitation". The flow between the kinetic and strain energy rates is "reactance cancellation": for a wing subjected to neither aerodynamic nor inertial loading (free vibration), the two terms will be equal and opposite.

This section concludes with a discussion of the analytically-computed design gradients computed via the methods outlined above. Two scalar functions are considered, averaged over the final flapping cycle once the behavior has become time-periodic: thrust coefficient (referencing Eq. (6), $g = C_{T,ave}$) and efficiency ($g = \eta$), which is given as the ratio of the average thrust to the average power [21]. The derivative of these two functions with respect to the thickness of each finite element (where the thickness is uniform, set to the value of 0.5 mm given in Table 1) is given in Fig. 7 for four cases. Case 1 (top row) assumes that the shell is clamped along the entire in-board section of the wing. This is not to say that this portion of the wing does not move; it is only clamped in the body-attached frame (xyz, Fig. 1). Motion along this boundary is entirely determined by the prescribed kinematics (Eq. (26)), and deformational motion ($\boldsymbol{u}$) is zero. Case 2 clamps the wing along the first quarter-chord of this boundary, case 3 along the entire leading edge, and case 4 along the first quarter-wing-length of the leading edge.

Lift and power coefficient gradients are not shown in Fig. 7, though both are computed in the framework described above (and power is obviously needed to compute η). As noted in Fig. 4, the time-averaged lift is consistently zero for the reciprocating motion described in Eq. (26), for both rigid and flexible wings. A redistribution of thickness will not change this, and so $\partial C_{L,ave}/\partial \boldsymbol{x}$ is a very small vector (due to temporal discretization errors) with little physical meaning. The power derivatives, conversely, were

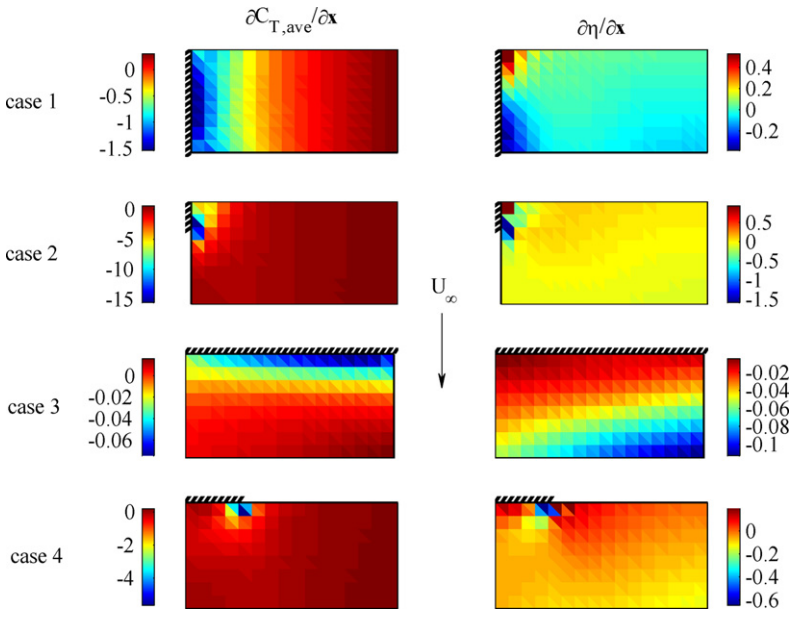

Fig. 7. Derivative of cycle-averaged thrust (right) and efficiency (left) with respect to finite element thicknesses for four boundary condition cases.

Table 2
Optimization results for peak thrust designs (Eq. (28)).

Case	$x_{\min}$	$x_{\max}$	Baseline			Optimum		
			$mass_o$	C_{T_o}	C_{p_o}	$mass$	$C_{T,ave}$	$C_{p,ave}$
1	0.3 mm	2 mm	7 g	0.3894	0.8813	6.997 g	0.4568	1.0749
2	0.3 mm	2 mm	7 g	0.4008	0.9060	6.981 g	0.5237	1.2463
3	0.15 mm	2 mm	7 g	0.3782	0.8519	6.992 g	0.3884	0.8947
4	0.35 mm	2 mm	7 g	0.3860	0.8701	6.981 g	0.4071	0.9233

not found to look significantly different from the thrust derivatives upon visual inspection: physical mechanisms that increase propulsion tend to also increase the required power input, highlighting the difficulties that arise in the design of efficient flapping wings. Minor differences in $\partial C_{T,ave}/\partial \boldsymbol{x}$ and $\partial C_{p,ave}/\partial \boldsymbol{x}$ are demonstrated in the efficiency derivatives of Fig. 7, which are much smaller in magnitude than the thrust derivatives for most of the cases.

For case 1, the gradients imply that propulsive thrust forces can be generated by decreasing the thickness at the root (where the stresses are largest), and increasing the thickness at the tip (where the inertial forces are largest). The combined effect should provide large bending deflections during the flapping stroke, whose deformational velocities have been shown (Fig. 4) to improve thrust. Efficiency, however, is improved with a stiff leading edge and a soft trailing edge. The resulting torsional motion should allow the wing to passively adapt to the airflow (washout), decreasing the overall angle of attack for power reduction [31]. Case 2 shows essentially the same design trends, though the influential finite elements are compressed into the clamped region along the first quarter-chord of the in-board region (as opposed to all along this boundary, as in case 1). As would be expected, the elements at the interface between the clamped edge and the free edge have a thickness which is very influential in the subsequent aeroelastic force generation.

The gradient trends seen in Fig. 7 for case 4 are not significantly different than that seen for case 2. This would indicate that the important physics governing the relationship between mass, stiffness, and aerodynamic forces are similar for the two cases. Despite the differences in orientation of the clamped boundary, both restraining mechanisms are located near the root, far from the location of peak inertial and aerodynamic load generation (wing tip). Case 3, however, which clamps the entire leading edge, has distinctly different design gradients. The thrust derivatives are that of case 1's, rotated by 90°: a softening of the wing along the clamped boundary, and an increase in mass along the opposite edge. This will increase the velocity (and hence the thrust) of the wing via larger chordwise bending deformations. Finite elements that lie closer to the wingtip have stronger derivatives, as the flapping motion is larger here. Efficiency derivatives for case 3 follow an opposite trend, decreasing the trailing edge thickness to allow for adaptive feathering during the stroke, as above.

6. Thrust and power optimization

Having provided a thorough description of the relevant interactions that govern the aeroelastic behavior of a flapping nonlinear shell, as well as the concomitant design gradients, focus is now turned to a series of optimization studies. For each of the boundary condition cases seen in Fig. 7, it is desired to solve two optimization problems. The first is formally stated as:

$$\max_{\boldsymbol{x}} g = C_{T,ave}$$
$$\text{s.t.:} \quad \begin{cases} x_{\min} < x_n < x_{\max}, \\ mass \leqslant mass_o, \end{cases} \qquad n = 1, \ldots, N_{DV} \tag{28}$$

where it is desired to maximize the cycle-averaged thrust of the wing, such that the mass of the wing is less than a baseline value (the mass of a wing with a uniform thickness of 0.5 mm, as noted in Table 1). Furthermore, the thickness of each finite element ($\boldsymbol{x}$) must lie between side constraints. The second optimization study, perhaps more relevant to flapping wing design [24], is:

$$\min_{\boldsymbol{x}} g = C_{p,ave}$$
$$\text{s.t.:} \quad \begin{cases} x_{\min} < x_n < x_{\max}, \\ mass \leqslant mass_o, \\ C_{T,ave} \geqslant C_{T_o}, \end{cases} \qquad n = 1, \ldots, N_{DV} \tag{29}$$

This second optimization problem seeks to minimize the cycle-averaged power of the wing, such that the same constraints as above are satisfied, as well as a thrust-based trim constraint (where C_{T_o} is the average thrust coefficient generated by a baseline flexible wing). A similar optimization problem would use maximum efficiency as an objective function, but this was not done here. Maximizing efficiency would provide the optimizer with some incentive to improve the thrust [21], when theoretically, only a certain amount of thrust is needed for trim. For Eq. (29), it is difficult to envision a situation where the minimum power design would not have an active thrust constraint.

In general, an additional series of constraints should also be imposed in order to ensure that the critical stress that develops within each shell finite element is below an acceptable threshold (see Ref. [18] for aeroelastic examples). This is particularly true when thickness variables are used, which have a substantial impact on the elastic stress distribution. These constraints are not explicitly included here however, but stress magnitudes are monitored during the design process and not found to be critical. The aeroelastic deformation of Fig. 5 provides a peak Von Mises stress of 25 MPa (at the root of the wing, during the large initial transients at $t/T = 0.4$), the largest value of any case studied below, yet still much less than the failure stress of carbon fiber plain weave composites (matrix cracking at 80 MPa). This is consistent with the behavior of highly flexible thin laminates, capable of large nonlinear displacements and rotations without failure.

Both optimization problems are solved for each boundary condition case, resulting in 8 total optimal thickness designs. Each is solved with the method of moving asymptotes [25], where the algorithm is provided with analytically-computed gradients for both the objective function and the constraints. Qualitative results are given in Tables 2 and 3, where the reported mass, thrust, and power is that for both wings (left and right). For the peak thrust designs (Table 2), the lower bound on thickness had to be limited (for cases 1, 2, and 4) to prevent divergence of the Newton–Raphson loop. As seen above, thrust can be greatly improved by substantial nonlinear wing deformations, which will test the convergence properties of the inner loop in Fig. 2. It should also be noted that the power metric is not included in the optimization processes of Table 2, but data is provided for completeness. The baseline design is, as discussed above, a uniform-thickness plate of 0.5 mm.

A typical optimization convergence history is given in Fig. 8, for the minimum power design of case 2. The MMA solver is seen to locate a minimum within 20 iterations, traveling along the thrust constraint boundary for the entirety of the process (variations in

Table 3
Optimization results for minimum power designs (Eq. (29)).

Case	$x_{\min}$	$x_{\max}$	Baseline			Optimum		
			$mass_o$	C_{T_o}	C_{p_o}	$mass$	$C_{T,ave}$	$C_{p,ave}$
1	0.15 mm	2 mm	7 g	0.3894	0.8813	4.5611 g	0.3896	0.8531
2	0.15 mm	2 mm	7 g	0.4008	0.9060	3.6321 g	0.4009	0.8533
3	0.15 mm	2 mm	7 g	0.3782	0.8519	2.1077 g	0.3817	0.8396
4	0.15 mm	2 mm	7 g	0.3860	0.8701	3.4785 g	0.3861	0.8467

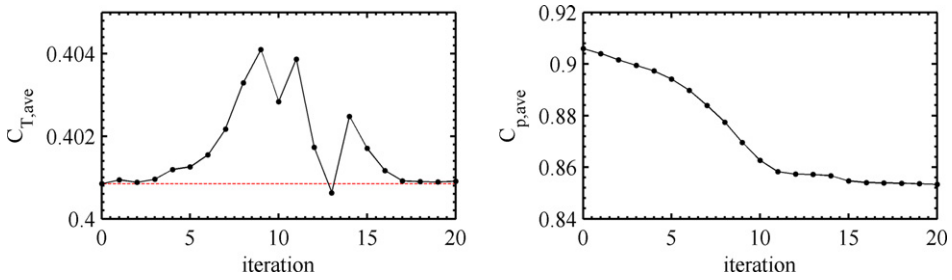

Fig. 8. Convergence history: minimum power design for case 2.

thrust during the optimization are very small). Some general observations can be made at this point, though a detailed discussion of the optimal results (for some of the interesting cases in Tables 2 and 3) will be given below. For the thrust-optimized results, the mass constraint is always active, owing to the usefulness of increasing the thickness in various portions of the wing for greater inertial forces, and thus greater bending velocities for thrust enhancement. Moderate improvements in the thrust coefficient are seen in Table 2, with up to a 30% improvement (case 2). The required power input increases as well however, resulting in a net drop in efficiency for each case.

For the power-optimized results (Table 3), the mass constraint is never active, as light-weight flexible structures are conducive to efficient passive shape adaptation, as well as lower inertial power requirements. The thrust constraint is generally active (as discussed above), with the exception of case 3, where the optimizer is able to simultaneously improve both thrust and power. The overall improvements in the objective function are lower than above (up to 5.2% power drop for case 2), and net efficiency necessarily increases for each case in Table 3, with a peak improvement of 6.2% for case 2. These modest power and efficiency gains may be due to the fact that Eq. (29) is a constrained optimization problem while Eq. (28) is not (and is thus easier to solve), or due to the relatively coarse mesh used to map the thickness distribution, which may struggle to adequately define the topological features of low-power designs (described below). Furthermore, the power-optimal designs in Table 3 (as well as the thrust-optimal designs of Table 2) may be local, as opposed to global optimum. The relatively large number of design variables precludes any definite conclusion as to this point, and a different baseline design may lead to an optimal design with a larger power drop than 5.2% for case 2, for example, due to the potential existence of multiple local minima. A detailed study of disparate baseline designs is not provided here however, where basic relationships between thrust-optimality, power-optimality, and thickness distributions are sought.

The optimal thickness distributions for case 1 are given in Fig. 9. The topological details of the peak thrust design follows the corresponding design gradients (Fig. 7) closely: the thickness at the root is dropped to the minimum gauge, the thickness at the tip is increased as far as the mass-constraint will allow. The thickness of the power-optimal design is also similar to the efficiency gradients at the root, though a diagonally-oriented batten is additionally present along the mid-portion of the wing. This latter structure is not discernible in any of the gradients shown above, which is indicative of the strongly nonlinear relationship between the aerodynamic force/power generation and the stiffness/mass distribution of the aeroelastic wing.

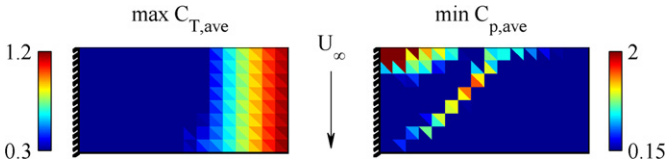

Fig. 9. Optimal thickness distributions (mm) for case 1.

Phase plots of the thrust and power coefficients are plotted as a function of β in Fig. 10, for the two thickness distributions in Fig. 9, as well as the baseline flexible design. Only the final, time-periodic flapping cycle is given, with an arrow to indicate the direction of the phase loop. Deformation at the trailing edge wing tip for the same cases can be seen in Fig. 11, in terms of the out-of-plane displacement and torsional twist. The thrust-optimal design is able to improve the propulsion over the baseline design only through the mid-stroke, for reasons noted above. Despite the large bending deformation at stroke reversal, little change in thrust is achieved. The quantified data of Table 3 indicates that the power-optimal and the baseline designs have the same time-averaged thrust (i.e., active trim constraint); Fig. 10 shows that the thrust at each time step is nearly identical as well.

The power-optimal design is able to decrease the time-averaged power (as seen in Table 3), but also the peak power draw required during the flapping cycle, which may be equally important in the design of flapping wings [26]. This drop is due to two factors: the diagonally-oriented batten adds negative bend–twist coupling to the wing structure. This is clearly seen in Fig. 11, where the positive bending deformation at the end of the upstroke (which is much lower than the bending of the thrust-optimal wing) corresponds to a negative wing twist of 4°, and vice-versa at the end of the downstroke. The resulting passive shape adaptation is able to alleviate the aerodynamic forces and power. The baseline and thrust-optimal designs show very little twisting throughout the flapping stroke, as these structures have negligible chordwise variations in stiffness/mass. Peak twist for these two cases occurs closer to the mid-stroke, and is due to the aerodynamic pitching moment, rather than elastic/inertial forces.

A second factor behind the success of the power-optimal design in Fig. 9 is the aforementioned drop in inertial power. A significant portion of the thickness of this design is at the minimum allowable

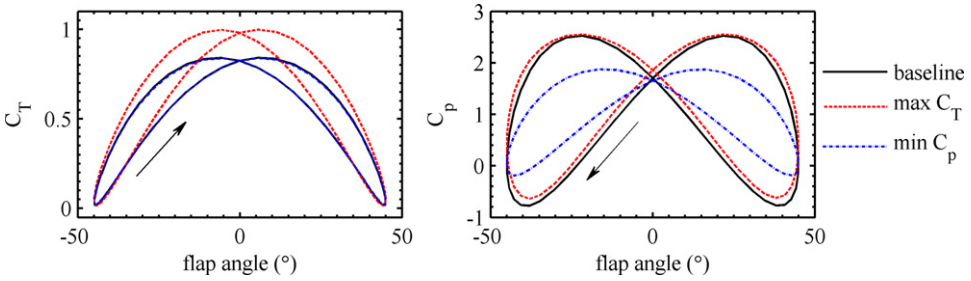

Fig. 10. Time-periodic thrust and power phase plots for case 1.

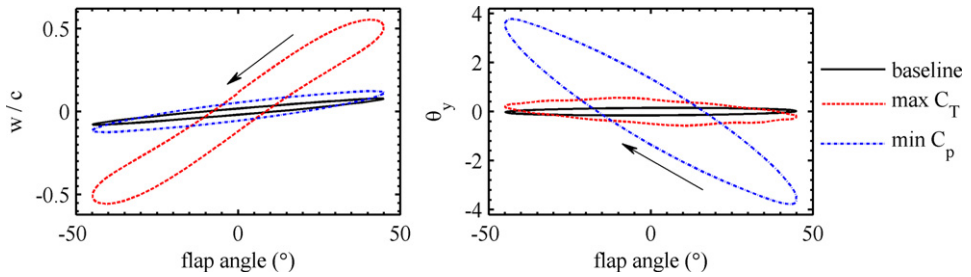

Fig. 11. Time periodic deformational displacement (left) and twist (right) at the trailing edge wingtip for case 1.

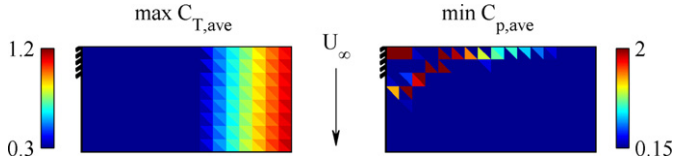

Fig. 12. Optimal thickness distributions (mm) for case 2.

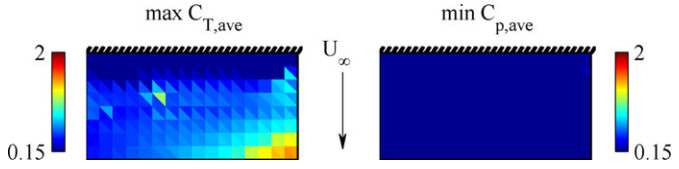

Fig. 13. Optimal thickness distributions (mm) for case 3.

gauge, which decreases the moment of inertia. For the reciprocating kinematics considered here (Fig. 1) inertial forces (and the corresponding power) along the body-attached z-axis will be equal and opposite during the two half strokes, and so should have no bearing upon the optimization problem of Eq. (29), which only considers time-averaged quantities. The inertial power due to centripetal forces along the y-axis will have the same sign during both strokes however, and will thus benefit, in a time-averaged sense, from a reduction in thickness.

The optimal thickness distributions for case 2 are given in Fig. 12, where it can be seen than the important topological details have not changed from case 1. The thrust-optimal design is nearly identical, and the diagonally-oriented batten now travels from the leading edge to the quarter-chord location of the in-board wing boundary, as opposed to the trailing edge (Fig. 9). The important physics behind the optimal designs has not greatly changed from the previous case (though the thrust-optimal design is now capable of sizable twisting deformations, due to the partially-clamped boundary), and will not be discussed in detail. It should also be mentioned that the flexible wing results in Figs. 3–6 were taken from the thrust optimal design of case 2.

The optimal thickness distributions for case 3 are given in Fig. 13, with the corresponding tip deformation in Fig. 14. Both the thrust- and power-optimal designs follow the topological trends set by the baseline gradients of Fig. 7; the latter, as all of its power gradients are negative, has an optimal thickness distribution that lies entirely along the lower gauge (0.15 mm). The resulting chordwise bending deformation (and adaptive feathering) is moderate, but is able to simultaneously increase the thrust and decrease the power (the only power-optimal design for which the thrust constraint is inactive, Table 3). Lumping more mass at the trailing edge doubles the magnitude of the deformation for thrust enhancement, but results in an increased power draw as well. It should be noted that the aeroelastic optimization of case 3 will be less successful if only because the relevant length scale (the chord) is less than the length scale for the previous two cases (the wing length) by a factor of two. Comparatively, this reduces the general magnitude of the wing deformation substantially, as noted in the baseline behavior of Fig. 14.

The optimal designs of the final case considered here can be seen in Fig. 15, though as noted in the discussion pertaining to the gradients of Fig. 7, the topological features are largely the same as

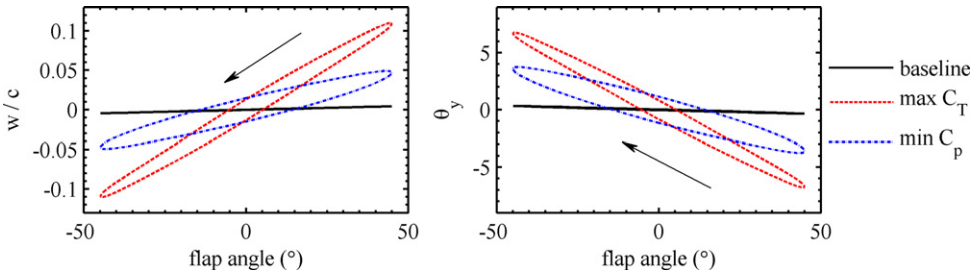

Fig. 14. Time periodic deformational displacement (left) and twist (right) at the trailing edge wingtip for case 3.

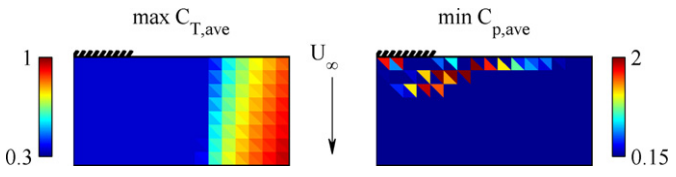

Fig. 15. Optimal thickness distributions (mm) for case 4.

case 2's, despite the difference in boundary conditions. A slight exception to this is that the thrust-optimal thickness distribution has a stronger chordwise gradient, with more mass grouped toward the trailing edge.

7. Conclusions

The thrust- and power-optimal thickness distributions of flexible flapping wings have been investigated. This is done via a numerical framework where a nonlinear shell model (a corotational approximation of the updated Lagrangian approach) is coupled to an unsteady vortex lattice method with a time evolving wake structure. The system response is computed with an implicit time marching scheme, with two nested loops within each time step to accommodate various coupled nonlinearities. Analytical design derivatives are then computed; specifically the gradient of an aerodynamic force/power quantity with respect to a large vector of thickness design variables, a vector whose cross-disciplinary nature emphasizes the coupled nature of the problem. This is done with a direct approach, formulating a second differential equation for the design gradients which is linear, with time-varying coefficients and multiple right-hand sides (one per design variable).

Two gradient-based optimization studies are considered (peak thrust, or minimum power under trim), for four different plate boundary conditions, resulting in 8 total cases. The following conclusions can be drawn, with reference to the summarizing Fig. 16:

1. For the baseline case, the relative size of the wing deformation at stroke reversal and through the mid-stroke provides a general idea as to the magnitude ratio of inertial to aerodynamic forces. For this work, the former is roughly three times larger than the latter.
2. Peak aerodynamic forces are generated near the mid-stroke, with positive thrust generated during both half-strokes (via a rotation of the lift vector). Large bending deformations have little effect upon the aerodynamic load redistribution, though the velocity caused by this motion (generally in-phase with the flapping velocity), can significantly increase the lift and thrust. Twisting deformations can alter the physical angle of attack (and thus the forces), though this was generally not as important as the bending velocity effects.
3. The mass constraint is always active for the thrust-optimized designs, due to the usefulness of increased inertial forces for propulsion. Up to a 30% improvement in thrust is available through thickness tailoring, though the required power consumption increases as well, resulting in a net drop in efficiency.
4. The mass constraint is never active for the power-optimal designs, due to a need for flexible, light-weight designs with low moments of inertia. The thrust constraint is generally active for trim, and as a result only moderate improvements in power consumption are available ($\sim 5\%$), though efficiency always increases.
5. Despite the differences in the boundary conditions of cases 1, 2, and 4, the topological details of the thrust or power designs do not vary significantly (though the magnitude of the aeroelastic behavior will differ). Peak thrust is generated by lowering the thickness at the root for increased flexibility, and increasing the thickness at the tip for increased inertial forces. The resulting behavior has a large bending velocity through the midstroke, increasing the thrust. Minimum power is generated by lowering the thickness to the lower bound, with the exception of a diagonally-oriented batten structure. The resulting wing has negative bend–twist coupling, in order to passively adapt to the flow.
6. Case 3 utilizes chordwise bending for peak thrust in much the same manner that the other cases use spanwise bending. The power-optimal design brings each thickness variable to its lower bound: the resulting feathering motion is able to simultaneously decrease power and increase thrust.

Future work for this research topic would necessarily include work conducted with higher-fidelity aeroelastic modeling (i.e., Navier–Stokes solvers) as well as a posteriori experimental validation of the optimal design discussed above. Regarding the former point, viscous effects are a particular concern, and it is desired to ascertain whether their inclusion into the optimization process would drastically alter the design trends outlined above. For example, it has been noted [30] that a primary goal of aeroelastic

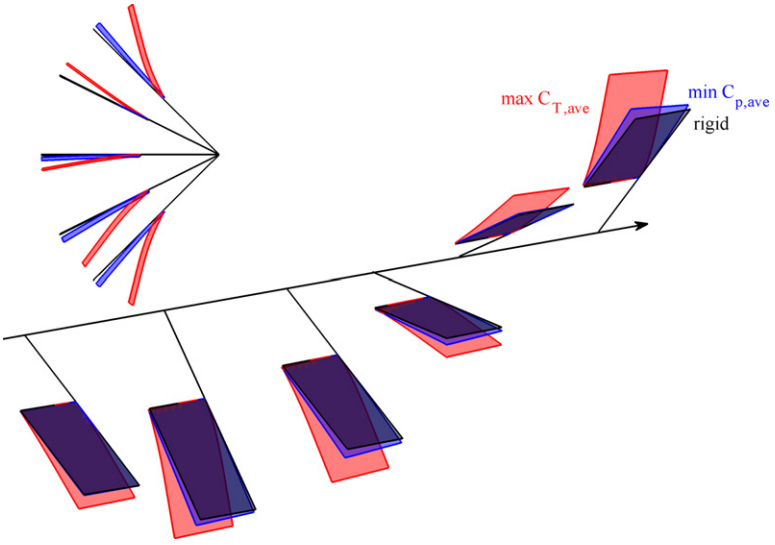

Fig. 16. Several snapshots of case 2 throughout the upstroke.

deformation during insect flight is to prevent the separation of flow from the wing surface. The adaptive washout of the power-optimal structures (Fig. 16) should be amenable to this as well, though post-processing of this design with a viscous aeroelastic solver, or (preferably) re-optimizing the wing structure with viscous effects included is required to assess the impact of these complex physics. Furthermore, the generation of aerodynamic lift during flapping flight involves the interaction of periodic vortex shedding from the leading and trailing edges, as well as the generation of a stable leading edge vortex with spanwise swirling [11]. Though none of the optimization studies given above include lift-based objective functions or constraints, their efficacy through an inviscid solver should also be assessed with higher fidelity modeling tools. Finally, experimental validation of the optimized designs (through either moderate or high fidelity means) is required, in order to ascertain which areas of the design space can be correctly described by moderate fidelity, low-cost tools.

Acknowledgements

This work is sponsored by the Air Force Office of Scientific Research under Laboratory Tasks 09RB01COR (monitored by Dr. Doug Smith) and 03VA01COR (monitored by Dr. Fariba Fahroo). The research was performed while the first author held a National Research Council Associateship Award at AFRL.

References

[1] P. Beran, G. Parker, R. Snyder, M. Blair, Design analysis strategies for flapping wing micro air vehicles, in: International Forum on Aeroelasticity and Structural Dynamics, Stockholm, Sweden, June 18–20, 2007.
[2] S. Chimakurthi, C. Cesnik, B. Stanford, Flapping wing structural dynamics formulation based on a co-rotational shell finite element, AIAA Journal 49 (1) (2010) 128–142.
[3] S. Combes, T. Daniel, Flexural stiffness in insect wings II. Spatial distribution and dynamic wing bending, Journal of Experimental Biology 206 (2003) 2989–2997.
[4] S. Combes, T. Daniel, Into thin air: Contributions of aerodynamic and inertial-elastic forces to wing bending in the hawkmoth *Manduca Sexta*, Journal of Experimental Biology 206 (2003) 2999–3006.
[5] R. Cook, D. Malkus, M. Plesha, R. Witt, Concepts and Applications of Finite Element Analysis, Wiley, New York, 2002.
[6] M. Dickinson, Directional sensitivity and mechanical coupling dynamics of campaniform sensilla during chordwise deformations of the fly wing, Journal of Experimental Biology 169 (1992) 221–233.
[7] T. Fritz, L. Long, Object-oriented unsteady vortex lattice method for flapping flight, Journal of Aircraft 41 (6) (2004) 1275–1290.
[8] R. Haftka, Z. Gürdal, Elements of Structural Optimization, Kluwer Academic Publishers, Dordrecht, The Netherlands, 1992.
[9] M. Hamamoto, M. Ohta, K. Hara, T. Hisada, Application of fluid–structure interaction analysis to flapping flight insects with deformable wings, Advanced Robots 21 (1) (2007) 1–21.
[10] S. Heathcote, Z. Wang, I. Gursul, Effect of spanwise flexibility on flapping wing propulsion, Journal of Fluids and Structures 24 (2) (2008) 183–199.
[11] S. Ho, H. Nassef, N. Pornsinsirirak, Y. Tai, C. Ho, Unsteady aerodynamics and flow control for flapping wing flyers, Progress in Aerospace Sciences 39 (8) (2003) 635–681.
[12] K. Isogai, Y. Harino, Optimum aeroelastic design of a flapping wing, Journal of Aircraft 44 (6) (2007) 2040–2048.
[13] J. Katz, A. Plotkin, Low-Speed Aerodynamics, Cambridge University Press, Cambridge, UK, 2001.
[14] N. Kim, K. Choi, Design sensitivity analysis and optimization of nonlinear transient dynamics, Mechanics of Structures and Machines 29 (3) (2001) 351–371.
[15] D. Kuhl, M. Crisfield, Energy-conserving and decaying algorithms in non-linear structural dynamics, International Journal for Numerical Methods in Engineering 45 (5) (1999) 569–599.
[16] H. Luo, B. Yin, H. Dai, J. Doyle, A 3D computational study of the flow–structure interaction in flapping flight, in: AIAA Aerospace Sciences Meeting, Orlando, FL, January 4–7, 2010.
[17] E. Madenci, A. Barut, Dynamic response of thin composite shells experiencing nonlinear elastic deformations coupled with large and rapid overall motions, International Journal for Numerical Methods in Engineering 39 (16) (1998) 2695–2723.
[18] J. Martins, J. Alonso, J. Reuther, A coupled-adjoint sensitivity method for high-fidelity aero-structural design, Optimization and Engineering 6 (1) (2005) 33–62.
[19] M. Platzer, K. Jones, J. Young, J. Lai, Flapping-wing aerodynamics: Progress and challenges, AIAA Journal 46 (9) (2008) 2136–2149.
[20] B. Singh, I. Chopra, Insect-based hover-capable flapping wings for micro air vehicles: Experiments and analysis, AIAA Journal 46 (9) (2008) 2115–2135.
[21] B. Stanford, P. Beran, Analytical sensitivity analysis of an unsteady vortex lattice method for flapping wing optimization, Journal of Aircraft 47 (2) (2010) 647–662.
[22] B. Stanford, P. Beran, Cost reduction techniques for the structural design of nonlinear flapping wings, in: AIAA Structures, Structural Dynamics, and Materials Conference, Palm Springs, CA, May 4–7, 2009.
[23] B. Stanford, P. Beran, Formulation of analytical design derivatives for nonlinear unsteady aeroelasticity, in: AIAA Structures, Structural Dynamics, and Materials Meeting, Orlando, FL, April 12–15, 2010.
[24] B. Stanford, M. Kurdi, P. Beran, A. McClung, Shape, structure, and kinematic parameterization of a power-optimal hovering wing, in: AIAA Structures, Structural Dynamics, and Materials Meeting, Orlando, FL, April 12–15, 2010.
[25] K. Svanberg, The method of moving asymptotes – a new method for structural optimization, International Journal for Numerical Methods in Engineering 24 (2) (1987) 359–373.
[26] T. Tantanawat, S. Kota, Design of compliant mechanisms for minimizing input power in dynamic applications, Journal of Mechanical Design 129 (10) (2007) 1064–1075.
[27] S. Thomson, Shape optimization and fluid dynamic analysis of a translating flexible body, in: AIAA Aerospace Sciences Meeting, Orlando, FL, January 4–7, 2010.
[28] T. Wasfy, A. Noor, Computational strategies for flexible multibody systems, Applied Mechanics Reviews 56 (6) (2003) 553–613.
[29] H. Yoo, J. Chung, Dynamics of rectangular plates undergoing prescribed overall motion, Journal of Sound and Vibration 239 (1) (2001) 123–137.
[30] J. Young, S. Walker, R. Bomphrey, G. Taylor, A. Thomas, Details of insect wing design and deformation enhance aerodynamic function and flight efficiency, Science 325 (5947) (2009) 1549–1552.
[31] Q. Zhu, Numerical simulation of a flapping foil with chordwise or spanwise flexibility, AIAA Journal 45 (10) (2007) 2448–2457.